ADVANCED OPTICAL MATERIALS
www.advopticalmat.de

Fabrication and Optical Characterization of CMOS-Compatible Honeycomb-Like Large-Scale Lattices of Near-Field Coupled Plasmonic TiN Nanotriangles

Jon Schlipf, Maria Alessandra Cutolo, Costanza Lucia Manganelli, Sebastian Reiter, Götz Seibold, Oliver Skibitzki, Christian Wenger, and Inga Anita Fischer*

Honeycomb-like plasmonic titanium nitride nanotriangle arrays defined by photolithography and fabricated in a modified silicon-germanium electronic–photonic integrated circuit process in a state-of-the-art pilot line. The nanotriangle arrays are characterized in experiments and simulations. The momentum-dependent reflectance spectra exhibit not only features that are consistent with surface lattice resonances in the honeycomb lattice but also minima governed by near-field coupling of the individual nanotriangles. The optical characterization results in combination with simulation-based predictions indicate that such nanotriangle arrays are capable of supporting collective plasmonic resonances that can be described as massless Dirac particles. The fabrication approach opens up the possibility of integrating the structures into device fabrication processes, and avenues toward near-infrared sensing and communication applications are predicted.

1. Introduction

Plasmonic excitations in single metallic nanoparticles and nanoparticle arrays have been widely investigated for their properties in tuning light-matter interaction at the nanoscale. Metallic nanoparticles can support collective oscillations of the electron gas, so-called localized surface-plasmon resonances (LSPR), upon excitation with light at the resonance frequency. When the nanoparticles are arranged in ordered lattices, the coupling between particles can lead to the appearance of collective resonances. In this case, optical properties such as peak position and peak width of resonances in the optical spectra are not only determined by the geometric properties of the individual particles but also by the lattice geometry,[1,2] i.e., lattice symmetry, lattice pitch, and inter-particle distance. Depending on inter-particle distance, two regimes can be identified.[3–5] In the diffractive regime, i.e., in the case of large inter-particle distances, collective modes result from the coupling of LSPR to diffractive orders (DO), propagating along the lattice surface as a result of the periodic arrangement of the nanoparticles (Rayleigh anomalies). These collective modes are called surface lattice resonances (SLR). Conversely, for inter-particle distances far below λ, i.e., in the evanescent regime, collective effects are dominated by coupling between neighboring particles via their overlapping evanescent fields. Tight-binding models that take only nearest-neighbor interactions into account have been employed to simulate, e.g., the resulting band structure.[6–8]

In 2D materials such as graphene, a honeycomb lattice of carbon atoms, the presence of fermionic massless Dirac quasiparticles in the band structure leads to a rich variety of uncommon phenomena such as nontrivial Berry phase accumulation.[9] There is interest in exploring the optical analogies of such honeycomb 2D materials in non-trivial photonic lattices similarly dominated by nearest-neighbor interactions. Near-field coupled nanoparticles arranged in plasmonic honeycomb lattices have been theoretically predicted to support Dirac-like plasmons[6–8,10] and topological edge states.[11] Furthermore, the optical properties of vertical stacking of such honeycomb plasmonic lattices as optical analogs of stacked graphene have been investigated based on simulation.[12] The nanofabrication of large areas of honeycomb plasmonic lattices with inter-particle distances low enough to address the near-field regime, however, remains challenging. So far, near-field coupled plasmonic nanoparticles in 1D chains have been experimentally realized, and edge states have been

J. Schlipf, C. L. Manganelli, O. Skibitzki, C. Wenger
IHP-Leibniz-Institut für Innovative Mikroelektronik
15236 Frankfurt (Oder), Germany
E-mail: schlipf@ihp-microelectronics.com
J. Schlipf, S. Reiter, I. A. Fischer
Chair of Experimental Physics and Functional Materials
BTU Cottbus-Senftenberg
03046 Cottbus, Germany
M. A. Cutolo
Optoelectronic Division-Engineering Department
University of Sannio
Benevento 82100, Italy
G. Seibold
Chair of Computational Physics
BTU Cottbus-Senftenberg
03046 Cottbus, Germany

DOI: 10.1002/adom.202403408

investigated in a honeycomb lattice containing comparatively few (up to 16) near-field coupled metallic nanoparticles.[13–16] Experimental investigations of extended 2D honeycomb lattices of metallic nanoparticles have been largely restricted to the diffractive regime, in which a tight-binding model description is insufficient to describe the system response, and the optical band structure is dominated by diffractive orders of the lattice.[1,2,4,7] Honeycomb plasmonic lattices in the diffractive regime have, e.g., been explored as open cavities to induce K-point[17] and M-point[18] lasing. In the diffractive regime, the influence on SLR peak shapes, in particular width, has been experimentally found to be negligible in the comparison of honeycomb lattices with square and hexagonal lattices under illumination at vertical incidence.[1] Other investigations have found increased peak heights in extinction spectra obtained from honeycomb lattices compared to hexagonal lattices under illumination at non-vertical incidence.[2]

Here, we report on the use of optical deep ultraviolet (DUV) lithography and etching to fabricate a large-scale array of triangular titanium nitride (TiN) nanoparticles arranged on two interpenetrating hexagonal lattices, which belongs to the same crystallographic space group *p6m* as the infinite honeycomb lattice. TiN offers metallic optical properties in the near-infrared range and has been explored for various plasmonic applications during the last decade. In contrast to noble metals generally preferred in plasmonics, TiN is easier to structure, more affordable, and chemically compatible with complementary metal-oxide-semiconductor (CMOS) processes.[19,20] TiN, thus, is particularly interesting for the integration of plasmonic nanostructures into electronic and photonic technologies. Despite lower carrier concentrations with respect to gold and silver, TiN has shown similar performance in metamaterials.[19,21] Among other applications,[20] titanium nitride plasmonic structures have been investigated for use in metalenses,[22] waveguiding,[23] and refractive index sensing.[24,25]

The 3×3 mm^2 large array investigated here is obtained from an industrial, CMOS-compatible fabrication process, which yields interparticle distances of ≈60 nm. We discuss the optical band structure in the context of SLR as well as a tight-binding approach. Importantly, we find evidence that strong near-field interactions between neighboring nanoparticles are at the origin of collective plasmonic resonances in our arrays. The excellent agreement between experiment and simulation highlights the advantages of using industrial fabrication processes for the fabrication of such structures.

2. Results and Discussion

Our TiN nanoparticle arrays with footprints of 3×3 mm^2 were obtained by introducing two minor modifications into the processing steps used for the top-down fabrication of hexagonal nanohole arrays with a pitch of 600 nm in a 200 mm wafer CMOS-compatible silicon (Si) technology processing line. In this process (see section "Experimental Section" for technical details), the nanotriangles are structured into a 150 nm TiN layer on a 200 nm silicon dioxide (SiO_2) layer on a Si substrate by a combination of DUV lithography and dry etching. Our fabrication process has previously been shown to yield TiN layers with low surface roughness and nanostructures with near-vertical sidewalls.[24] The first modification targeted the mask used for DUV lithography, where we defined arrays with a constant pitch of 600 nm and varying hole diameters of 390, 450, and 510 nm. The separation between neighboring holes with diameters of 510 nm on the lithography mask is only 90 nm, this is already at the resolution limit for the DUV lithography with a wavelength of $\lambda = 248$ nm used in our process and leads to a distortion of the shape of the holes via proximity effects. The second modification targeted the etching time, which was chosen to exceed the minimum time required to etch a TiN layer with a thickness of 150 nm by a factor of ≈1.5, leading to overetching. As a result of both modifications, the nanoholes in arrays with a nominal hole diameter of 510 nm grew sufficiently large to touch each other, and we observed the formation of triangular islands of TiN (**Figure 1**). Additional, larger-scale images of the nanotriangle array can be found in Figure S1 (Supporting Information). A transition between hexagonal nanotriangle and nanohole arrays has previously been reported only for nanosphere lithography,[26–28] however, nanotriangle arrays produced in that manner are susceptible to fabrication imperfections, impacting long-range order in large arrays. Here, our structures were obtained based on an entirely CMOS compatible fabrication process[29,30] as the most cost-effective approach that, at the same time, is able to generate large-scale arrays in a reproducible and scalable manner. We note that alternative lithography techniques such as electron beam lithography and nanoimprint lithography can achieve a better spatial resolution, and are expected to yield sharper corners and smaller gaps. This could, in turn, strengthen the near-field coupling effects we intend to study. However, masked lithography delivers superior throughput and scalability, which has encouraged recent efforts in exploiting the advantages in particular of DUV lithography for metasurface fabrication.[31–34] Furthermore, with our top-down fabrication approach, we are able to obtain TiN nanotriangles with a height of 150 nm, enabling sizeable out-of-plane dipole moments to be excited. Achieving high spatial resolution with electron beam lithography often requires the resist thickness to be low, limiting etching times or requiring the structuring of metal layers with a lift-off process. In both cases, this leads to metal nanostructures with reduced thicknesses, in which dipole moments may be largely confined to in-plane orientations.

While the use of DUV lithography for the fabrication of the TiN nanoparticle arrays nominally limits structural sizes, the corner-to-corner separation distance of 60 nm is well below the resolution limit expected for a wavelength of $\lambda = 248$ nm used during exposure. The limitations of our lithography step as well as of the plasma etching step, which has small variations over the wafer, lead to the introduction of defects in the form of imperfect separations between adjacent triangles (Figure 1c). We expect further optimizations in the lithography and etch process parameters to reduce these defects. However, we do not consider the defects a major issue in our system, as experiments and simulations – which neglect defects – show very similar trends.

We consider LSPR of an individual nanotriangle as the starting point of our investigation of the optical properties of our structures. In order to understand the single-particle LSPR, we conducted finite-difference time-domain (FDTD) and finite element method (FEM) simulations for plane-wave excitation. The material permittivity used in the simulation was obtained from spectroscopic ellipsometry measurements of our sputtered TiN

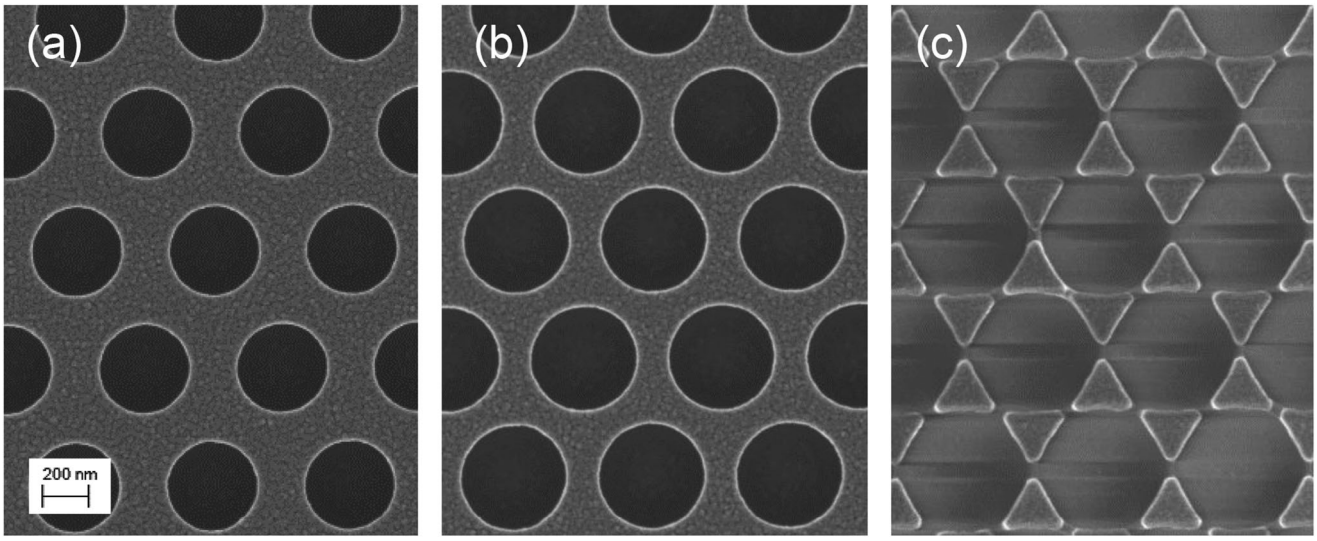

Figure 1. Scanning electron microscope image of the fabrication results from NHA lithography with constant array pitch of 600 nm and nominal (measured) hole diameters of a) 390 (391) nm b) 450 (469) nm, and c) 510 (–) nm.

layers and is shown in Figure S2 (Supporting Information). A detailed analysis has also been reported in ref. [24] For the primary dipole mode, both absorption and scattering cross-sections peak at 1125 nm (**Figure 2**). For increasing corner radius, the peaks blueshift, toward 1000 nm for the case of 50 nm corner radius. Simulated electric field distributions (Figure 2) allow us to attribute these peaks to the dipole mode of the nanotriangles, with poles at each end of one edge of the triangle in the case of x-parallel electric field excitation (Figure 2c)). The field distribution for y-parallel excitation (Figure 2d)) has one pole at one tip and at the edge opposite to it. Due to the vertical incidence and the symmetry properties of the triangle, the scattering and absorption cross-sections are independent of polarization.[35] This is because any incoming plane wave can be written as a linear combination of plane waves polarized at 0°, 120°, and −120° relative to the *x*-axis of the lattice. As the geometry is invariant under these rotations, so are the wave propagation problem and its solutions.

It is worth noting that rounding of the corners of the triangle, which occurs in fabrication, can have a large influence on the amplitude and position of the dipole-related cross-section peak (Figure 2a,b). We observed a corner radius of ≈10 nm in our fabricated TiN nanotriangles and used this value in all subsequent simulations.

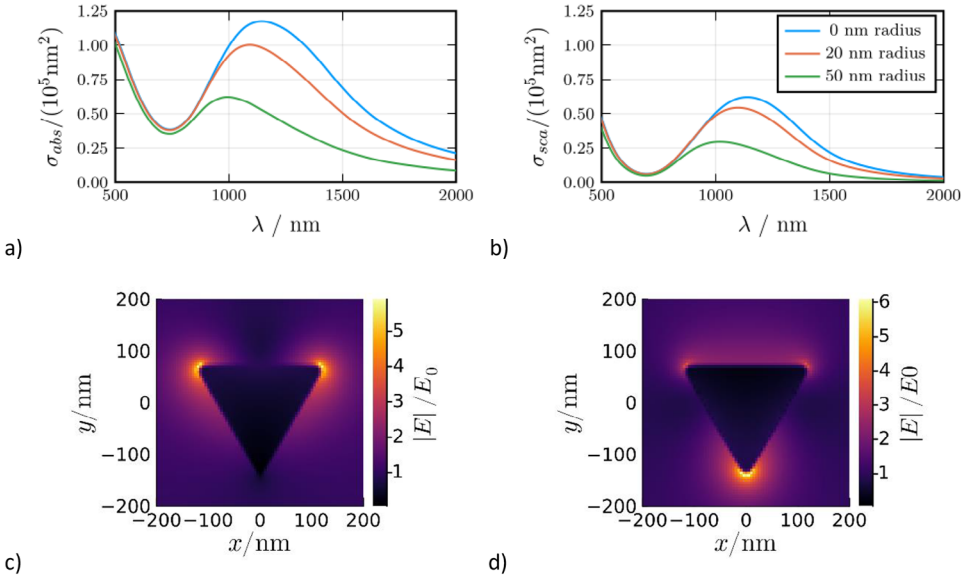

Figure 2. FDTD simulated a) absorption and b) scattering cross-sections of single TiN nanotriangles with an edge length of 250 nm for different corner radii and polarizations. FDTD simulated electric field distribution (absolute value normalized to source excitation amplitude) for plane-wave (total field/scattered field) excitation at 1124 nm with polarization in parallel with the c) *x*-axis and d) *y*-axis of triangles with a corner radius of 10 nm.

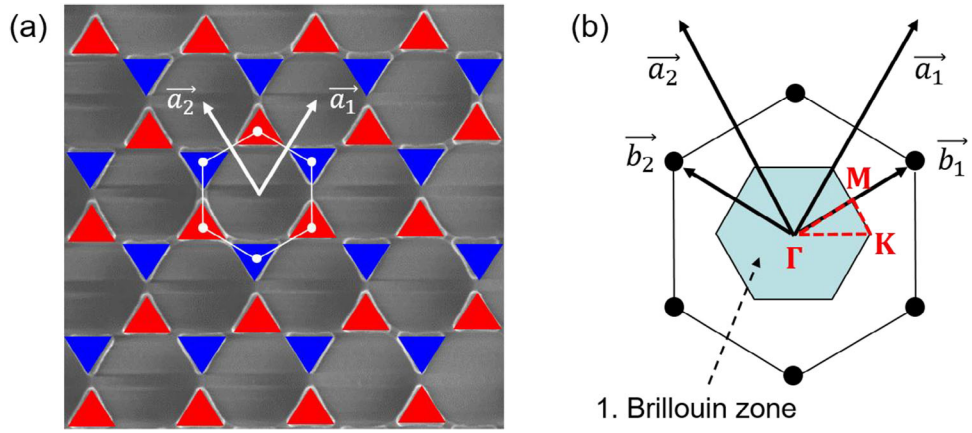

Figure 3. a) Schematic overlay of the unit cell of the honey-comb lattice on a scanning electron microscope image of the nanostructures. b) First Brillouin zone with the critical Γ, *K*, and *M* points.

Placing the TiN nanotriangles in arrays of two interpenetrating hexagonal lattices can be expected to modify optical properties. While limited to far-field excitation, measuring and simulating the reflection of plane waves by the structure as a function of wavelength and angle of incidence provides insights into the dispersion relation and, thus, the nature of interactions between the elements of the lattice. Far-field probing of modes is possible if the incident light can couple to a dipole moment, as in our case. Substrate effects tend to play a role in the mediation of the coupling.[18,36–38] We investigated the dispersion relations in both simulation and experiment. To this end, we simulated the reflectance of our device geometry under transverse-magnetic (TM) polarized incidence by rigorous coupled-wave analysis (RCWA) as a function of photon energy E and the in-plane component of the wave vector $k_{||} = \left|\vec{k}\right| \sin\theta$. $k_{||}$. $k_{||}$ was set in parallel with the Γ-*K* and Γ-*M* lines of the first Brillouin zone of the lattice, respectively (**Figure 3**).

We compared the simulated data with interpolated experimental reflectance spectra measured under TM polarized grazing incidence at angles of incidence between 5° and 50° in increments of 5°. The experimental data were interpolated numerically in order to plot a map of measured reflectance on the rectilinear momentum-energy grid. For K- and M- oriented incidence (**Figure 4**), we see agreement between the heatmaps of simulated (left) and measured (right) reflectance. This corroborates our simulation approach. Experimental data are only available for angles of between 5° and 50°, bordered by the red lines. Orange lines show the maximum possible angle of incidence at 90°.

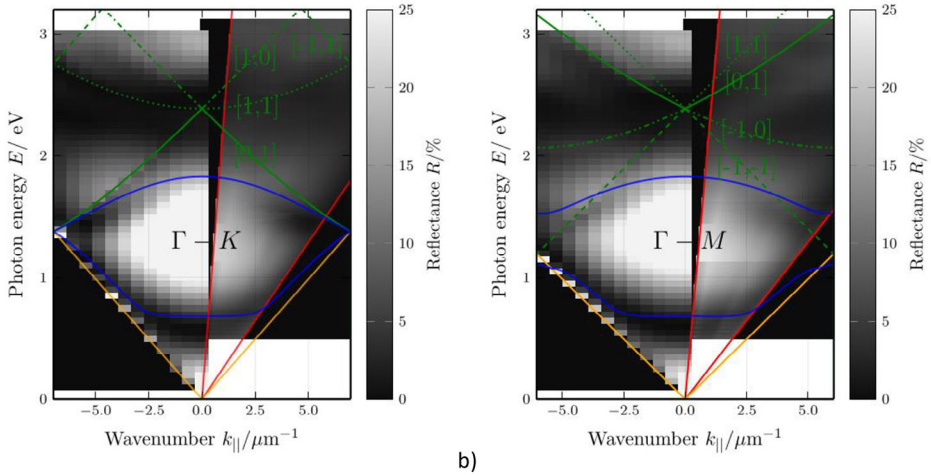

Figure 4. Simulated (left) and experimentally measured (right) reflectance (0th diffraction order) of a honeycomb-like TiN nanotriangle array as a function of photon energy and in-plane wavenumber. $k_{||}$ was set in parallel with a) the Γ-*K* line and b) the Γ-*M* line of the first Brillouin zone. The triangles have a center-center distance of $600/\sqrt{3}$ nm, and an edge length of 250 nm. The corners are rounded with a radius of 10 nm. The green lines show where the momentum matching condition required for SLR excitation is fulfilled, with indices *i* and *j* denoted in brackets for each line. The blue lines mark the dispersion resulting from a tight-binding model for the coupled nanotriangles.

The heatmap plots also show the SLR dispersion lines related to several critical points of the Brillouin zone $\vec{G}_{i,j}$, of a honeycomb lattice, with the momentum matching condition

$$E\left(\vec{k}_{||}\right) = \hbar\left|\vec{k}_{||} + \vec{G}_{i,j}\right| cn \tag{1}$$

here, $\hbar$ is the reduced Planck's constant, c is the speed of light in vacuum, n is the refractive index of the superstrate (free space in this case), and $\vec{k}_{||}$ is the projection of the wave vector on the array plane. For photon energies above 2.5 eV, one can observe contours and extrema in reflectance matching the dispersion lines. We note that the real part of the permittivity of TiN is negative only for wavelengths above 650 nm (see Figure S2, Supporting Information), i.e., the material is no longer metallic in this regime. We nonetheless take the match as confirmation of the correspondence of our lattice to the honeycomb lattice.

For photon energies below 2 eV, the observed spectral features cannot be fully explained with the SLR lattice dispersion. In a previous investigation of the transition from nanohole arrays to nanotriangle arrays by Murray et al.,[26] spectral positions of resonances in spectra obtained from the nanotriangle arrays showed only negligible dependence on $\vec{k}_{||}$ and were attributed to the presence of LSPRs of uncoupled triangles. By contrast, our spectra show a clear dependence of the spectral positions of reflectance minima on $\vec{k}_{||}$ in that wavelength range. As we discuss in the following, we take this as evidence for the existence of collective plasmonic modes originating from the near-field coupling between the nanoparticles as a result of both the small separation between individual triangles and the structural homogeneity of the 3×3 mm^2 large array. Indeed, placing the nanoparticles in an array configuration as shown in Figure 3a, with separations of 60 nm between corners of adjacent nanotriangles, ensures coupling between neighboring dipole modes via their overlapping evanescent fields. The following dispersion was obtained by Weick et al.[6] for a honeycomb lattice of near-field coupled metallic nanospheres described by point dipoles:

$$E\left(\vec{k}_{||}\right) = \hbar\omega_0\sqrt{1 \pm \frac{\Omega}{\omega_0}\left[\sum_{j=1}^{3} C_j e^{i\vec{k}_{||}\cdot\vec{e}_j}\right]} \tag{2}$$

here, $\vec{e}_j$ are the connection vectors to the three nearest neighbor atoms in the lattice. ω_0 is the resonance frequency of individual nanoparticles and Ω describes the coupling strength between triangles. The coefficients C_j are direction-dependent coupling terms corresponding to the three nearest neighbors of a nanotriangle. As the shape of our nanoparticles differs from the spheres discussed by Weick et al.,[6] we used the following, modified expression for C_j

$$C_j = 1 - 3a\sin(\theta)^2\cos\left(\varphi - 2\pi\frac{j-1}{3}\right)^2 \tag{3}$$

here, θ is the angle of incidence, φ is the azimuthal angle, and the parameter a is used to empirically take into account the out-of-plane anisotropy of the nanotriangles. We chose $a = 0.2$ in order to obtain a good fit between the dispersion curves and the minima in the simulated and experimental reflectance spectra. A more detailed discussion can be found in the Supporting Information.

The dispersion curves obtained from a tight-binding approach provide a good match to the minima in both the simulated and the experimental reflectance spectra for photon energies between 0.5 and 2 eV. As a consequence of our choice of parameters, the presence of Dirac-like, massless collective plasmonic resonances is predicted at the K point in momentum space, while a gap is predicted to open up at the M point. We emphasize that the presence or absence of gaps depends on numerical values for the parameters and should be verified by a more detailed calculation, which we do not present here. Our results nonetheless strongly indicate that nanotriangle array configurations obtained from our CMOS-compatible fabrication process are capable of supporting collective plasmonic resonances originating from near-field coupling of the nanotriangles. It should also be mentioned here that the presence of massless collective plasmonic resonances requires a thickness of the TiN layer (150 nm in our case), which allows for the existence of non-negligible out-of-plane dipoles in the nanotriangles

To facilitate quantitative comparison between measurement and simulation as well as dispersion relations from SLR resonances and the tight-binding model the measured and simulated reflectance spectra for an angle of incidence of 35° toward the K point of the lattice are shown in **Figure 5a**. The vertical black lines show the positions of surface lattice resonances (see Equation 1). The blue lines show the wavelengths corresponding to the dispersion of the near-field coupled lattice. Peaks in the experiment and simulation match qualitatively. As can be clearly seen in the simulated reflectance spectrum, the derivative of the spectrum shows a discontinuity at $\lambda = 750$ nm, coinciding with the SLR dispersion. The dispersion relation obtained from a tight-binding approach, however, provides a better match for the lowest-energy minimum in the reflectance spectrum, thus corroborating our claim that optical properties of the honeycomb-like lattice of TiN nanotriangles are dominated by near-field interactions between neighboring nanoparticles. It has to be noted that for wavelengths above ≈2000 nm (corresponding to photon energies below ≈0.62 eV) the nanotriangles do not support strong electric dipoles (Figure 2a,b), whereas for wavelengths below ≈650 nm (corresponding to energies above ≈1.9 eV) the real part of the permittivity of TiN becomes positive (Figure S2, Supporting Information) – as a result, a description of the dispersion relation of the honeycomb-like lattice of TiN nanotriangles in terms of near-field interaction between electric dipoles in metallic nanoparticles can only be valid at intermediate wavelengths.

Further insight can be obtained by comparing the reflectance heat maps of the honeycomb-like nanotriangle arrays (Figure 4) with reflectance heat maps of hexagonal nanohole arrays with a pitch of 600 nm (**Figure 6**). This transition leads to marked differences in reflectance spectra for photon energies below 2 eV. These differences can also be clearly observed in Figure S3 (Supporting Information), where results for nanohole and nanotriangle arrays are shown in the same graph. Not only is there a clear difference in the wavelength-dependent position of reflectance minima, but the presence of pronounced reflectance minima at positions defined by Equation (1) in the case of the nanohole array is a clear indication of the strong influence of Rayleigh anomalies on optical properties in these arrays. Plots of the electric fields

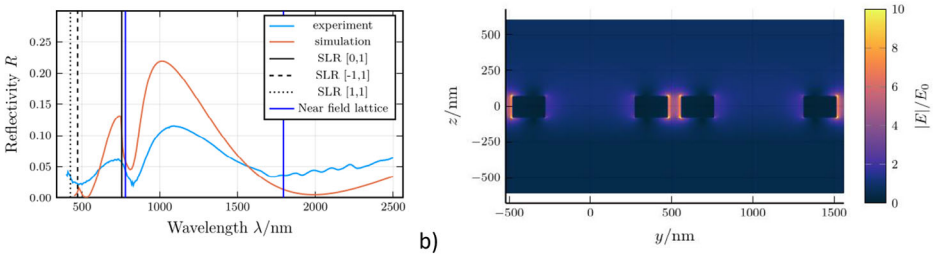

Figure 5. a) Simulated and measured reflectance spectra (0th diffraction order) of the nanotriangle array under illumination with TM polarized light for an angle of incidence of 35°, toward the *K* point of the first Brillouin zone. b) Simulated near fields for a section through the tips of triangles for vertical incidence, $\lambda = 2\mu m$.

at wavelengths corresponding to reflectance dips under vertical incidence are shown in Figure 5b and Figure S6 (Supporting Information).

Simulation results for the cases of both floating (substrate-free) nanostructures and a bulk silicon substrate without oxide film can be found in Figures S4 and S5 (Supporting Information). Importantly, the dispersion relations close to the K and M points of the floating nanostructures and the samples discussed here have very similar shapes. While the influence of a Si substrate on the reflectance spectra is strong, owing to its large refractive index, the reflectance spectra of the honeycomb-like lattice of nanotriangles and those of hexagonal nanohole arrays nonetheless remain very dissimilar in all cases. Again, we emphasize that a description based on near-field interactions is only valid in the range between 0.62 and 1.9 eV.

Finally, we note that our nanotriangle array also belongs to the class of geometrically frustrated structures, in which competing dipole-dipole interactions between adjacent particles cannot be satisfied simultaneously.[39,40] Extending the description of near-field coupling between individual triangles, we briefly discuss an approach in analogy with a Potts model in the Supporting Information to describe the nearest-neighbor interactions between triangles in a finite array when illuminated with unpolarized light.

3. Conclusion

We have demonstrated the fabrication of large honeycomb-like arrays of plasmonic nanotriangles using a CMOS-compatible fabrication process. Our characterization, based on measured and simulated reflectance spectra, strongly indicates that the optical properties of those arrays are shaped by near-field interactions of electric dipoles induced in the individual nanotriangles. Such arrays can potentially support Dirac plasmonic excitations at selected points of the Brillouin zones.

Combined with the mature silicon photonics fabrication process, robustness with respect to fabrication tolerances makes the arrays showcased here ideal candidates for the application of near-field coupled plasmonic honeycomb-like lattices and their unique properties. With the fabrication process established, it is also possible to investigate smaller-scale arrays, especially with respect to edge modes[11,41] with the aim of employing the resulting optical effects together with integrated photonic devices. Wafer-scale fabrication also allows for the accurate fabrication of large-scale, multilayer structures, enabling additional degrees of freedom in analogy, e.g., to bi- or multilayer graphene. Also, the precision of the foundry process can be exploited for the fabrication of two or more stacked plasmonic metasurfaces with a well-defined twist relative to each other. Such twisted stacks, known

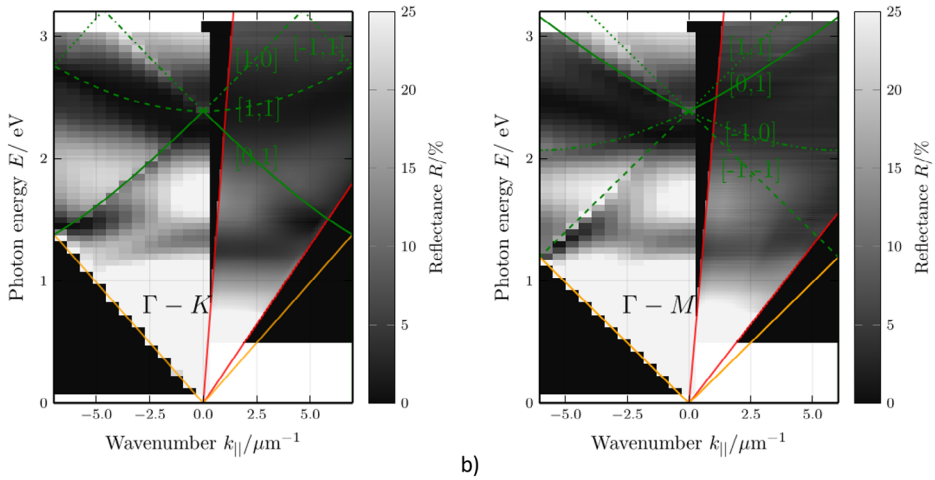

Figure 6. Simulated (left) and measured (right) reflectance (0th diffraction order) of a hexagonal TiN nanohole array as a function of photon energy and in-plane wavenumber. $k_{||}$ was set in parallel with a) the Γ-*K* line and b) the Γ-*M* line of the first Brillouin zone. The nanoholes have a center-center distance of 600 nm and a diameter of 510 nm. See the caption of Figure 4.

as moiré metasurfaces, have recently attracted interest, showing several effects as a photonic analogy to twisted bilayers of 2D materials.[42,43]

In order to efficiently predict the properties of fabricated arrays, further refinement, numerical verification, and application of the tight-binding model is required. We also note that, while this fabrication process makes use of well-established deposition and etching processes for TiN, which results in vertical sidewalls and low roughness, TiN is known to exhibit strong damping compared to several other CMOS-compatible metallic materials such as, e.g., aluminum and it would be interesting to apply this fabrication process to aluminum and leverage its superior plasmonic properties for applications.

4. Experimental Section

The nanotriangle array was dry etched into a layer stack of 150 nm of TiN on 200 nm of SiO_2 on a silicon substrate, in a slightly modified version of IHP's silicon-germanium electronic-photonic integrated circuit (EPIC) technology and described elsewhere[24,29,30] The relevant steps and thicknesses of the TiN and SiO_2 layers were identical to the ones used in our full foundry process, where TiN nanohole arrays were combined with germanium (Ge) photodetectors for future applications in biosensing.[29] Fabrication of the samples investigated here started from a p-doped (100) Silicon (Si) wafer with dopant concentration $N_A = 10^{15}$ cm^{-3} as a substrate, onto which a SiO_2 layer with a thickness of 200 nm was deposited using a plasma-enhanced chemical vapor deposition (PECVD) process with tetraethyl orthosilicate (TEOS) as a precursor. As a next step, a 150 nm thin TiN film was deposited by DC magnetron sputtering. Lithography was performed using a spin-coated positive resist with a thickness of 325 nm, without anti-reflective coating. After patterning the resist with a deep UV stepper, the TiN was etched in an inductively coupled plasma reactive ion etch (ICP-RIE) system using a Cl_2/Ar mixture and an etching time of 100 s. This etching time exceeded the minimum time required for the etching of the full TiN layer (70 s). As a result, the hole diameters were slightly increased to the point where the holes touch in hexagonal arrays with a pitch of 600 nm and nominal hole diameter of 510 nm, leaving behind the triangular islands of TiN, as shown in Figure 1c).

Vertical-incidence reflectance of the samples was studied by Fourier Transform Infrared Spectroscopy using a Bruker Vertex 80 with Bruker Hyperion 2000 microscope. Grazing-incidence reflectance was measured in a PerkinElmer LAMBDA 1050 UV/VIS/NIR with a total absolute measurement system (TAMS) accessory and an InGaAs detector. Reflectance was measured for both TE and TM polarization in a wavelength range of 400–2500 nm.

5. Modeling and Simulation

The FEM simulations in COMSOL Multiphysics[44] were performed with the Electromagnetic Waves model in the frequency domain. To reduce the computational domain, exploiting the symmetry of the system, the simulated structure consists of the unit cell of the nanoantenna array. All refractive index data was taken from measured experimental values. We simulated with a triangular mesh with an average quality factor of 0.63. For the simulation of arrays, the structure was illuminated with a linear polarized source (E||x), and we applied Floquet boundary conditions in the lateral dimensions in order to match experimental data. For the simulation of individual triangles, we applied scattering boundary conditions.

We use FDTD simulation[45] both for additional modeling of the polarizability of single nanotriangles along with FEM and for the simulation of infinite arrays. For all simulations, we worked with a uniform 2 nm mesh and uniaxial perfectly matched layers. Permittivity data for Si and SiO_2 were supplied with the software tools, and we used a dispersive model extracted from our own data for TiN.

We model the dispersion of the honeycomb lattice with the rigorous coupled wave analysis (RCWA).[46] We consider a maximum order of 12 for the discrete 2D Fourier series in spatial frequency. We use literature permittivity data for Si[47] and SiO_2,[48] and inhouse measured permittivity data for TiN. TiN permittivity spectra can be found in Figure S2 (Supporting Information).

Supporting Information

Supporting Information is available from the Wiley Online Library or from the author.

Acknowledgements

The authors would like to thank the Federal Ministry of Education and Research of Germany (BMBF) for financial support under the "Innovationscampus Elektronik und Mikrosensorik – iCampµs Cottbus" project, grant numbers 16ME0424K and 16ES1131. The authors are grateful to M. Fritscher for support with the high-performance computing cluster at IHP, and D. Stolarek and P. Nitsch for scanning electron and optical microscopy.

Conflict of Interest

The authors declare no conflict of interest.

Data Availability Statement

The data that support the findings of this study are available from the corresponding author upon reasonable request.

Keywords

honeycomb lattice, optical dirac point, plasmonics, silicon photonics, titanium nitride

Received: December 11, 2024
Revised: May 26, 2025
Published online: June 14, 2025

[1] A. D. Humphrey, W. L. Barnes, *Phys. Rev. B* **2014**, *90*, 075404.
[2] R. Guo, T. K. Hakala, P. Törmä, *Phys. Rev. B* **2017**, *95*, 155423.
[3] A. O. Pinchuk, G. C. Schatz, *Mater. Sci. Eng., B* **2008**, *149*, 251.
[4] R. Kolkowski, A. F. Koenderink, *Proc. IEEE* **2020**, *108*, 795.
[5] H. Yu, Q. Sun, J. Yang, K. Ueno, T. Oshikiri, A. Kubo, Y. Matsuo, Q. Gong, H. Misawa, *Opt. Express, OE* **2017**, *25*, 6883.
[6] G. Weick, C. Woollacott, W. L. Barnes, O. Hess, E. Mariani, *Phys. Rev. Lett.* **2013**, *110*, 106801.
[7] F. Fernique, G. Weick, *Phys. Rev. B* **2020**, *102*, 045420.
[8] T. J. Sturges, C. Woollacott, G. Weick, E. Mariani, *2D Mater.* **2015**, *2*, 014008.

[9] A. H. Castro Neto, F. Guinea, N. M. R. Peres, K. S. Novoselov, A. K. Geim, *Rev. Mod. Phys.* **2009**, *81*, 109.
[10] D. Han, Y. Lai, J. Zi, Z.-Q. Zhang, C. T. Chan, *Phys. Rev. Lett.* **2009**, *102*, 123904.
[11] L. Wang, R.-Y. Zhang, M. Xiao, D. Han, C. T. Chan, W. Wen, *New J. Phys.* **2016**, *18*, 103029.
[12] D. Becerril, G. Pirruccio, C. Noguez, *Phys. Rev. B* **2021**, *103*, 195412.
[13] A. Poddubny, A. Miroshnichenko, A. Slobozhanyuk, Y. Kivshar, *ACS Photonics* **2014**, *1*, 101.
[14] C. W. Ling, M. Xiao, C. T. Chan, S. F. Yu, K. H. Fung, *Opt. Express, OE* **2015**, *23*, 2021.
[15] I. S. Sinev, I. S. Mukhin, A. P. Slobozhanyuk, A. N. Poddubny, A. E. Miroshnichenko, A. K. Samusev, Y. S. Kivshar, *Nanoscale* **2015**, *7*, 11904.
[16] Q. Yan, E. Cao, X. Hu, Z. Du, Y. Ao, S. Chu, Q. Sun, X. Shi, C. T. Chan, Q. Gong, H. Misawa, *Nanophotonics* **2022**, *11*, 3495.
[17] R. Guo, M. Nečada, T. K. Hakala, A. I. Väkeväinen, P. Törmä, *Phys. Rev. Lett.* **2019**, *122*, 013901.
[18] X. G. Juarez, R. Li, J. Guan, T. Reese, R. D. Schaller, T. W. Odom, *ACS Photonics* **2022**, *9*, 52.
[19] G. V. Naik, J. L. Schroeder, X. Ni, A. V. Kildishev, T. D. Sands, A. Boltasseva, *Opt. Mater. Express, OME* **2012**, *2*, 478.
[20] U. Mahajan, M. Dhonde, K. Sahu, P. Ghosh, P. M. Shirage, *Mater. Adv.* **2024**, *5*, 846.
[21] C.-C. Chang, J. Nogan, Z.-P. Yang, W. J. M. Kort-Kamp, W. Ross, T. S. Luk, D. A. R. Dalvit, A. K. Azad, H.-T. Chen, *Sci. Rep.* **2019**, *9*, 15287.
[22] J. Hu, X. Ren, A. N. Reed, T. Reese, D. Rhee, B. Howe, L. J. Lauhon, A. M. Urbas, T. W. Odom, *ACS Photonics* **2017**, *4*, 606.
[23] N. Kinsey, M. Ferrera, G. V. Naik, V. E. Babicheva, V. M. Shalaev, A. Boltasseva, *Opt. Express, OE* **2014**, *22*, 12238.
[24] S. Reiter, W. Han, C. Mai, D. Spirito, J. Jose, M. Zöllner, O. Fursenko, M. A. Schubert, I. Stemmler, C. Wenger, I. A. Fischer, *Plasmonics* **2023**, *18*, 831.
[25] S. Reiter, M. Ratzke, P.-G. Nitsch, C. Mai, D. Spirito, A. A. Corley-Wiciak, C. Wenger, I. A. Fischer, *Plasmonics* **2025**.
[26] W. A. Murray, S. Astilean, W. L. Barnes, *Phys. Rev. B* **2004**, *69*, 165407.
[27] D. Correia-Ledo, K. F. Gibson, A. Dhawan, M. Couture, T. Vo-Dinh, D. Graham, J.-F. Masson, *J. Phys. Chem. C* **2012**, *116*, 6884.
[28] A. Colombelli, D. Lospinoso, R. Rella, M. G. Manera, *Nanomaterials* **2022**, *12*, 547.
[29] C. Mai, S. Marschmeyer, A. Peczek, A. Kroh, J. Jose, S. Reiter, I. Fischer, C. Wenger, A. Mai, *ECS Trans.* **2022**, *109*, 35.
[30] C. Mai, A. Peczek, A. Kroh, J. Jose, S. Reiter, C. Wenger, I. A. Fischer, *Opt. Express, OE* **2024**, *32*, 29099.
[31] J. Seong, Y. Jeon, Y. Yang, T. Badloe, J. Rho, *Int. J. Precis. Eng. Manuf.-Green Tech.* **2024**, *11*, 685.
[32] A. Leitis, M. L. Tseng, A. John-Herpin, Y. S. Kivshar, H. Altug, *Adv. Mater.* **2021**, *33*, 2102232.
[33] G. Yoon, T. Tanaka, T. Zentgraf, J. Rho, *J. Phys. D: Appl. Phys.* **2021**, *54*, 383002.
[34] R. F. Wolffenbuttel, M. A. Ghaderi, *Photonics Nanostructures – Fundam. Appl.* **2022**, *51*, 101050.
[35] M. M. Islam, M. M. Hossen, T. Koschny, A. C. Hillier, *J. Phys. Chem. C* **2021**, *125*, 11478.
[36] Y. Moritake, M. Ono, M. Notomi, *Nanophotonics* **2022**, *11*, 2183.
[37] M. A. Gorlach, X. Ni, D. A. Smirnova, D. Korobkin, D. Zhirihin, A. P. Slobozhanyuk, P. A. Belov, A. Alù, A. B. Khanikaev, *Nat. Commun.* **2018**, *9*, 909.
[38] S. Fiedler, S. Raza, R. Ai, J. Wang, K. Busch, N. Stenger, N. A. Mortensen, C. Wolff, *Opt. Express, OE* **2020**, *28*, 13938.
[39] A. Conde-Rubio, A. F. Rodríguez, X. Borrisé, F. Perez-Murano, X. Batlle, A. Labarta, *Opt. Express* **2018**, *26*, 20211.
[40] A. Conde-Rubio, A. Fraile Rodríguez, A. Espinha, A. Mihi, F. Pérez-Murano, X. Batlle, A. Labarta, *Sci. Rep.* **2019**, *9*, 3529.
[41] M. Hafezi, S. Mittal, J. Fan, A. Migdall, J. M. Taylor, *Nat. Photon* **2013**, *7*, 1001.
[42] G. Hu, M. Wang, Y. Mazor, C.-W. Qiu, A. Alù, *Trends in Chemistry* **2021**, *3*, 342.
[43] M. Oudich, X. Kong, T. Zhang, C. Qiu, Y. Jing, *Nat. Mater.* **2024**, *23*, 1169.
[44] COMSOL Multiphysics® Software – Understand, Predict, and Optimize. COMSOL, https://www.comsol.com/comsol-multiphysics (accessed: September 2024).
[45] Nanophotonic FDTD Simulation Software – Lumerical FDTD. Lumerical, https://www.lumerical.com/products/fdtd/ (accessed: November 2020).
[46] J. Schlipf, I. A. Fischer, *Opt. Express, OE* **2021**, *29*, 36201.
[47] C. Schinke, P. Christian Peest, J. Schmidt, R. Brendel, K. Bothe, M. R. Vogt, I. Kröger, S. Winter, A. Schirmacher, S. Lim, H. T. Nguyen, D. MacDonald, *AIP Adv.* **2015**, *5*, 067168.
[48] I. H. Malitson, *J. Opt. Soc. Am., JOSA* **1965**, *55*, 1205.